Observations of nitric oxide in the Antarctic middle atmosphere during recurrent geomagnetic storms

David A. Newnham,[1] Patrick J. Espy,[2,3] Mark A. Clilverd,[1] Craig J. Rodger,[4] Annika Seppälä,[1,5] David J. Maxfield,[1] Paul Hartogh,[6] Corinne Straub,[2,7] Kim Holmén,[8] and Richard B. Horne[1]

[1] We report ground-based measurements of the polar middle atmosphere made using a 230–250 GHz passive microwave radiometer deployed at Troll station (72°01′S 02°32′E, L shell of $L = 4.8$), Antarctica. Our observations show enhanced mesospheric nitric oxide (NO) volume mixing ratio (VMR) during a series of small recurrent geomagnetic storms in the 2008 austral winter, reaching 1.2 ppmv on day 200 (18 July). The Lomb normalized periodogram of the NO VMR time series averaged over 65-80 km for days 130 to 220 of 2008 (9 May to 7 August) shows a peak exceeding the 95% confidence limit at 25.8 days, close to the synodic rotation period for low-latitude solar coronal holes. The highest correlations between the radiometer NO VMR data and trapped and quasi-trapped electron count rates for $L = 3.5\text{-}5.5$ from the Polar Orbiting Environment Satellites 90° telescope are for the $>30\,\text{keV}$ (90e1) channel ($r_{max} = 0.56$, lag time of 5.1 days) and $>100\,\text{keV}$ (90e2) channel ($r_{max} = 0.57$, lag time of 4.4 days). Maximum correlation between NO VMR and the $>700\,\text{keV}$ (90P6) channel data is lower but lag times are close to zero. Superposed epoch analyses for the eight most significant geomagnetic storm periods and three Carrington rotations (2070-2072) within the 90 day observation period indicate that significant NO abundance observed at 65-80 km in the Antarctic mesosphere may be produced directly by $>200\,\text{keV}$ electron precipitation or originate from a source at higher altitudes, e.g., production by $>30\,\text{keV}$ electrons followed by downward transport.

Citation: Newnham, D. A., P. J. Espy, M. A. Clilverd, C. J. Rodger, A. Seppälä, D. J. Maxfield, P. Hartogh, C. Straub, K. Holmén, and R. B. Horne (2013), Observations of nitric oxide in the Antarctic middle atmosphere during recurrent geomagnetic storms, *J. Geophys. Res. Space Physics*, *118*, 7874–7885, doi:10.1002/2013JA019056.

1. Introduction

[2] Production of the odd nitrogen (NO_x) species nitric oxide (NO) and nitrogen dioxide (NO_2) in the middle atmosphere by energetic electrons and protons, and its effect in chemically perturbing stratospheric ozone distributions, is well established [e.g., *Brasseur and Solomon*, 2005; *Sinnhuber et al.*, 2012]. In the thermosphere and upper

[1] British Antarctic Survey, Cambridge, UK.
[2] Department of Physics, Norwegian University of Science and Technology, Trondheim, Norway.
[3] Also at Birkeland Centre for Space Science, Bergen, Norway.
[4] Department of Physics, University of Otago, Dunedin, New Zealand.
[5] Also at Earth Observation, Finnish Meteorological Institute, Helsinki, Finland.
[6] Max Planck Institute für Solar System Research, Katlenburg-Lindau, Germany.
[7] Now at Swiss Federal Office for Statistics, Neuchâtel, Switzerland.
[8] Norwegian Polar Institute, Tromsø, Norway.

Corresponding author: D. A. Newnham, British Antarctic Survey, High Cross, Madingley Rd., Cambridge, England CB3 0ET, UK. (david.newnham@bas.ac.uk)

mesosphere, NO_x exists mainly as NO but below 65 km conversion to NO_2 occurs [*Solomon et al.*, 1982]. The chemical lifetime of NO_x in the sunlit mesosphere and lower thermosphere is typically 1 day [*Shimazaki*, 1984; *Solomon et al.*, 1999]. During the day, NO_2 is converted to NO either by reaction with atomic oxygen or by photolysis at wavelengths shorter than 405 nm. In the upper stratosphere and above, NO is photolyzed in the δ bands to generate $N(^4S)$. This reacts with NO, causing a loss of odd nitrogen during daytime. In darkness, NO_x has a lifetime of months and can be transported downward by the polar vortex at high latitudes during winter [*Siskind et al.*, 2000]. Atmospheric circulation models and reanalysis meteorological data have indicated that changes in ozone abundance due to NO_x arising from energetic particle precipitation can affect polar surface air temperatures by as much as 4 K [*Rozanov et al.*, 2005; *Seppälä et al.*, 2009; *Baumgaertner et al.*, 2011].

[3] Intense solar storms can greatly increase stratospheric NO_x abundance, leading to temporary $>60\%$ ozone loss and perturbing levels of trace species for up to 12 months [*Jackman et al.*, 2009]. Such solar proton events occur sporadically, last a few days, and deposit 1–500 MeV protons into the stratosphere and mesosphere over the polar caps. NO_x may be produced more frequently and persistently in

the polar middle atmosphere by energetic electron precipitation (EEP) from the Earth's magnetosphere than by solar protons [*Randall et al.*, 2005]. The processes by which these electrons impact stratospheric ozone and the role of atmospheric transport on those processes are uncertain. At geomagnetic latitudes of 70°-75°, high fluxes of low energy (1-10 keV) auroral electrons enter the atmosphere almost continuously and produce thermospheric NO in abundance at 110 km over the polar caps, even during low-geomagnetic activity [*Marsh et al.*, 2004]. In the subauroral zone (geomagnetic latitudes ≤70°), relativistic electrons that have been accelerated in the Van Allen radiation belts reach MeV energies [*Horne et al.*, 2005] and can penetrate down to the stratosphere. At intermediate energies, 10–100 keV electrons deposit most of their energy between 100 km and 75 km whereas ionization and NO_x/HO_x production by ~0.1–1 MeV electrons is greatest in the upper stratosphere and mesosphere [*Turunen et al.*, 2009]. The effects on atmospheric chemistry due to MeV electron precipitation are predicted to be more likely to occur in the Southern hemisphere (SH), poleward of the South Atlantic Magnetic Anomaly (SAA) region, and during the recovery phase of storms [*Horne et al.*, 2009].

[4] NO_x produced in the high-latitude middle atmosphere has the potential to be transported downward into the stratosphere by the Antarctic polar vortex between May and October [*Randall et al.*, 2007] and modulates ozone abundances [*Solomon et al.*, 1982; *Brasseur and Solomon*, 2005]. *Lee et al.* [2011] determined first empirical orthogonal function mode indices of CO in the SH winter and found the descent rates, constant at 0.16-0.2 km/day below 40 km, increase almost linearly with altitude above 40 km to ~1 km/day at 80 km. *Sheese et al.* [2011] determined a proxy NO descent rate in the Antarctic mesosphere and lower thermosphere of 3.8 km/day, somewhat larger than mean vertical wintertime wind speeds typically presumed to be ~2 cm/s (i.e., ~1.7 km/day). Meridional circulation reversal, which shows large wintertime variability and equatorward flow at 68°S above 80-98 km [*Hibbins et al.*, 2005; *Sandford et al.*, 2010], could provide a barrier preventing auroral NO from descending, although diffusion still plays a role [*Smith et al.*, 2011]. Thus, it is unclear whether NO produced at high altitudes (>90 km) by plentiful lower energy (1–30 keV) electrons, requiring substantial downward transport, is more important than NO_x produced at lower altitudes (<90 km) by high-energy (30 keV to several MeV) electrons [*Clilverd et al.*, 2009a]. Sudden stratospheric warmings can result in the breakdown of the Arctic wintertime polar vortex and disrupt the downward transport of NO_x. However, in some of these events, the stratopause and accompanying vortex has been observed to reform at higher altitudes and this can lead to the pronounced NO descent and NO_x enhancements sometimes observed at high latitudes in the Northern Hemisphere [*Randall et al.*, 2009].

[5] Satellite-based NO_x observations have also had issues in determining the origin of the observed enhancements. For example, a very significant doubling of NO_2 mixing ratio from ~47–70 km observed by Global Ozone Monitoring by Occultation of Stars (GOMOS) during mid-February 2004 was suggested to arise from in situ production by geomagnetic storm-induced relativistic electrons [*Clilverd et al.*, 2009a]. The NO_2 mixing ratio at northern polar latitudes observed by GOMOS increased 3 days after the start of a geomagnetic storm with moderate *Kp* and associated with corotating interaction regions/high-speed streams (CIR/HSS). The enhanced NO_2 abundance coincided with increased flux of relativistic electrons measured by Space Environment Monitor instruments on board the Geostationary Operational Environmental Satellites (GOES) and Polar Orbiting Environment Satellites (POES). The observed NO_2 mixing ratios were reproduced using atmospheric model calculations of ionization by ≥1.25 MeV electrons. Michelson Interferometer for Passive Atmospheric Sounding (MIPAS) measurements over a similar latitude range show strong increases of NO_x in the upper stratosphere and lower mesosphere around ~60 km in early 2004. However, correlations with tracer data show that this enhancement is more likely due to downwelling of NO_x from the upper mesosphere and lower thermosphere [*López-Puertas et al.*, 2006]. Furthermore, conclusions that can be drawn about the contribution of relativistic electrons to upper stratospheric or lower mesospheric NO_x from 15 years of Halogen Occultation Experiment data are limited by the lack of polar winter coverage by solar occultation measurements [*Sinnhuber et al.*, 2011].

[6] We have recently reported vertical profiles of ozone and NO, the original source of NO_x produced by energetic electrons, measured directly and with unprecedented temporal resolution by a new passive microwave radiometer located at the Norwegian Troll station (72°S, 2°E), Antarctica. From observations during small, relatively isolated geomagnetic storms between 2008 days 80 and 129 (20 March to 8 May), we identified that NO was produced directly in the mesosphere at 70-80 km by ~300 keV electron precipitation [*Newnham et al.*, 2011]. During a moderate geomagnetic storm (minimum *Dst* of −79 nT) in late July 2009, we observed a decrease of 20–70% in mesospheric ozone, coincident with increased NO, between 60 km and 75 km altitude associated with >30 keV energetic electron precipitation [*Daae et al.*, 2012]. By showing that significant NO production occurs even at an unusually quiet solar minimum, during which geomagnetic activity was exceptionally low, high-energy electrons under more typical geomagnetic conditions may be a much more important source of NO_x and have a larger impact on stratospheric ozone than previously thought. In order to address this, NO production in the mesosphere and stratosphere by energetic electrons needs to be better quantified and represented in global atmospheric models.

[7] Recurrent geomagnetic storms arising from CIR/HSS occur more frequently during solar minimum. The 2008–2009 solar minimum was a period of extremely quiet geomagnetic conditions [e.g., *Tsurutani et al.*, 2011; *Burns et al.*, 2012]. However, during this period, and particularly in 2008, long duration (~5-10 days) weak to moderate (minimum *Dst* index ≥ −50 nT) recurrent geomagnetic storms occurred [*Gibson et al.*, 2009].

[8] In this paper, we report ground-based measurements of NO in the Antarctic middle atmosphere during the austral winter between days 130 and 220 of 2008 (9 May to 7 August). We carry out statistical analyses to determine periodicities in mesospheric NO, an overlapping thermospheric NO data set, geomagnetic indices, and electron data. We use correlation lag and superposed epoch analyses to investigate the possible sources of observed mesospheric NO enhancements and production by EEP following recurrent geomagnetic storms.
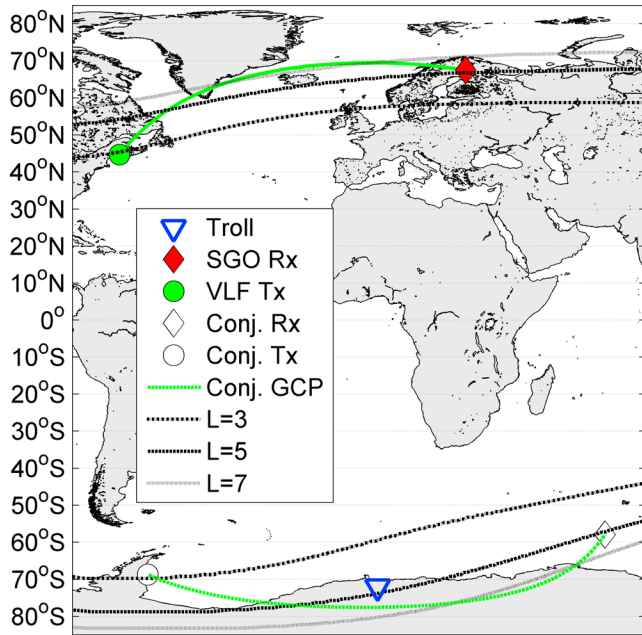
Figure 1. A map showing the location of Troll station, Antarctica, the subionospheric VLF propagation path from the NAA transmitter (VLF Tx) to the AARDDVARK SGO receiver (SGO Rx) in Finland, and the conjugate great circle path (GCP) in the Southern Hemisphere. Contours of constant L shell are shown for $L = 3$, 5, and 7.

2. Experimental Setup

2.1. Microwave Radiometer Observations

[9] The microwave radiometer used in this study has been described previously [*Espy et al.*, 2006; *Straub et al.*, 2013] and thus only the NO measurement details are given here. Ground-based atmospheric observations at a 60° zenith angle were made from Troll station, Antarctica (72°01′S, 02°32′E, 1275 m above sea level), the position of which is shown in Figure 1. Troll is at a geomagnetic latitude of 65°, suitable for observing the effects of EEP from the outer radiation belt, and it is also typically inside the Antarctic polar vortex which extends to at least 60°S from the pole and from the mesosphere down to the lower stratosphere [*Harvey et al.*, 2004].

[10] NO volume mixing ratio (VMR) profiles were inverted from calibrated brightness temperature spectra measured by a chirp transform spectrometer [*Hartogh and Hartmann*, 1990; *Villanueva and Hartogh*, 2004; *Villanueva et al.*, 2006] with 14 kHz resolution and 40 MHz bandwidth. For this analysis, 10 MHz sections of each daily mean average spectrum, centered on the NO line at 250.796 GHz, were inverted using the Microwave Observation Line Estimation and Retrieval version 5 code [*Urban et al.*, 2004]. A priori pressure, temperature, ozone, water vapor, and NO profiles above 30 km were calculated using the Sodankylä Ion and Neutral Chemistry (version 6.8) model [*Verronen et al.*, 2005] under geomagnetically quiet conditions. For altitudes up to 30 km, MIPAS/ Envisat (Michelson Interferometer for Passive Atmospheric Sounding/Environmental Satellite) data were combined with 10 year (1999-2008) averages of ozonesonde data from Neumayer station (70°39′S, 08°15′W). Spectroscopic reference data for radiative transfer calculations were taken from HITRAN (high-resolution transmission molecular absorption database) 2008 [*Rothman et al.*, 2009]. Data inversion was performed from the ground to 120 km with 1 km thick layers to ensure stable convergence. NO and tropospheric water vapor profiles were adjusted in the forward model calculations to provide the best fit to the observed brightness temperatures. Radiometer data with brightness temperatures above 150 K, caused by high levels of tropospheric water vapor and/or blowing snow, and negative VMR values were rejected.

2.2. AARDDVARK Electron Precipitation Observations

[11] The Antarctic-Arctic Radiation-belt Dynamic Deposition VLF Atmospheric Research Konsortium (AARDDVARK) receiver network [*Clilverd et al.*, 2009b] monitors the subionospheric transmission of narrowband very low frequency (VLF) radio wave signals in the 10 kHz to 40 kHz range originating from powerful communication transmitters located around the world. The VLF radio signals propagate in a waveguide formed by the Earth's surface and the bottom of the ionosphere (D region) located between 50 km and 100 km. Changes in the D region ionosphere modify the amplitude and phase of transmitted VLF signals [*Barr et al.*, 2000], allowing changes in the sources of ionization, such as particle precipitation, in the mesosphere-lower thermosphere to be monitored [see e.g., *Clilverd et al.*, 2009b and references therein].

[12] This study makes uses of the 24.0 kHz signals from the transmitter with the call sign NAA (Cutler, Maine, USA, 44°N, 67°W, $L = 2.9$) received at the Sodankylä Geophysical Observatory (SGO, 67°N, 26°E, $L = 5.1$) in Finland. The transmitter to receiver great circle path (GCP) and the L shell contours for $L = 3$, 5, and 7 are shown in Figure 1. The plot shows that VLF signals following the NAA to SGO GCP are influenced by EEP for $L = {\sim}3$-8. The NAA amplitude variation outside of the normal diurnal variability exhibited by the received VLF signal is driven primarily by electron precipitation associated with geomagnetic storms and has been compared with electron fluxes detected by the POES and DEMETER satellites [*Clilverd et al.*, 2010]. Following the approach outlined in that paper, we modeled the NAA amplitude variations in order to determine an integral electron precipitation flux for specific times of day and limited ranges of magnetic local time (MLT). Analysis of amplitude data from the 02:00-03:00 UT time period corresponds to precipitation occurring in the 22:00-06:00 MLT range, i.e., the midnight sector.

[13] The geomagnetic conjugate of the NAA to SGO great circle path has a SH footprint which passes close to Troll station. To a first approximation, the SH precipitating fluxes will be at least the same magnitude as those observed in the NH for 30 keV electrons, and possibly electrons with energies as high as 300 keV, while larger fluxes of relativistic electrons could occur at the edge of the bounce loss cone over the SAA [*Meredith et al.*, 2011]. Here we use the well-modeled AARDDVARK NH data to estimate the >50 keV precipitating electron flux close to Troll.

2.3. POES and GOES Electron Observations

[14] Particle measurements are made by the Space Environment Monitor 2 (SEM-2) instrument packages on board the NOAA Polar Orbiting Environment Satellites (POES), which are in high-inclination Sun-synchronous orbits
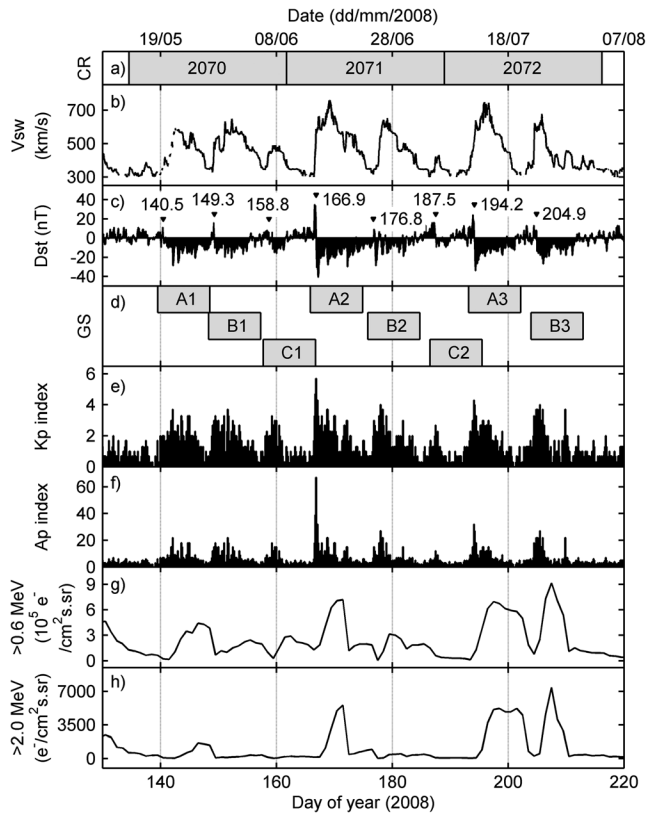
Figure 2. (a) Carrington rotation (CR) periods, (b) hourly solar wind velocity (*V*sw), (c) hourly *Dst* index and sudden storm commencements (inverted black triangles), (d) 9 day geomagnetic storm (GS) periods, (e) 3-hourly *Kp* index, (f), 3-hourly *Ap* index, and daily mean GOES electron flux at $L = 6.6$ for the (g) >0.6 MeV and (h) >2.0 MeV channels.

at altitudes of ~800-850 km. SEM-2 includes the Medium Energy Proton and Electron Detector (MEPED) and the Total Energy Detector (TED) that together monitor electron fluxes from 50 eV to 2.5 MeV [*Evans and Greer*, 2004; *Rodger et al.*, 2010]. MEPED has two electron telescopes and two proton telescopes. The electron telescopes point in approximately perpendicular directions (0° and 90°), are ±15° wide, and each provide three channels of energetic electron data: >30 keV, >100 keV, and >300 keV. In addition, omni-directional measurements are made by a dome detector ±60° wide, which is mounted parallel to the 0° detector. Poleward of geomagnetic latitude 33°, the 0° electron telescope monitors electrons in the bounce loss cone that will enter the Earth's atmosphere. At high latitudes, the MEPED 90° electron telescope measures trapped and quasi-trapped electrons (i.e., electrons in the drift loss cone that are not lost to the atmosphere locally but are lost in regions where the magnetic field is weaker) [*Rodger et al.*, 2010]. Contamination by comparatively low energy protons can be significant in the MEPED observations when the proton flux is high [*Rodger et al.*, 2010]. Typically, up to ~42% of the observations of >30 keV electrons using the 0° telescope are contaminated, but only ~3.5% of the corresponding 90° telescope observations are affected. For <300 keV electrons, the precipitation generally follows variations in the trapped flux [*Meredith et al.*, 2011], and we therefore use the 90° telescope

observations due to the lower levels of proton contamination. Here we use SEM-2 data with 2 s resolution from NOAA-15, NOAA-16, NOAA-17, and NOAA-18 plus MetOp-02 (available from http://www.ngdc.noaa.gov/stp/satellite/poes/dataaccess.html). We apply a proton correction algorithm (available from the Virtual Radiation Belt Observatory, http://virbo.org) to these data as described in *Lam et al.* [2010, Appendix A]. We then use these corrected data to determine daily mean electron count rates for the >30 keV (channel 90e1), >100 keV (channel 90e2), >300 keV (channel 90e3), and the larger than ~700 keV (channel 90P6) [*Yando et al.*, 2011] channels between $L = 3.5$ and 5.5.

[15] The Space Environment Monitor instrument on board the Geostationary Operational Environmental Satellite (GOES) provides >0.6 MeV and >2 MeV electron fluxes at a nominal fixed L shell of $L = 6.6$. The GOES >2 MeV channel responds primarily to trapped outer zone electrons. In practice, the geostationary orbit is not at a constant L and so we use daily mean average electron fluxes calculated from the daily electron fluence data from GOES-12 provided by the National Space Weather Prediction Center (see www.swpc.noaa.gov/ftpdir/indices/old_indices/2008_DPD.txt).

2.4. SABER NO Observations

[16] The Sounding of the Atmosphere using Broadband Emission Radiometry (SABER) instrument [*Mlynczak*, 1997] on the Thermosphere, Ionosphere, Mesosphere Energetics and Dynamics (TIMED) satellite measures atmospheric radiance profiles in 10 bands between 1.27 and 15 µm. We use zonal daily mean NO volume emission rate (VER) data for 65°-75°S, derived from SABER 5.3 µm channel observations [*Mlynczak et al.*, 2003]. Although SABER continuously scans the limb over the altitude range 0-350 km, the observed NO VER is dominated by processes occurring above 110 km. These data provide a measure of the thermospheric cooling rate but it is important to note that increases in NO VER may not correspond to increases in NO abundance. A number of processes contribute to increases in NO VER: (1) increases in NO abundance, leading to more vibrationally excited NO via collisions with atomic oxygen (O); (2) increases in kinetic temperature, which controls the rate of collisional excitation of NO via detailed balance with collisional quenching. A higher kinetic temperature means more excited NO molecules all else being equal; (3) exothermic production of vibrational levels of NO; and (4) increases in O abundance.

3. Results

3.1. Geomagnetic Indices, Solar Data, and GOES Data

[17] Three complete Carrington rotations (2070–2072, Figure 2a) occurred between 2008 days 130 and 220 (9 May to 7 August). During this period, solar activity was very low with the visible disk spotless for much of the time and only isolated low-level B-class flares detected on day 138. No solar proton events were observed at geosynchronous orbit.

[18] Solar wind velocity data (available from http://umtof.umd.edu/pm/crn/) from the Advanced Composition Explorer are shown in Figure 2b. The periods of increased velocity, with low values in between, are typical of recurrent CIR/HSS. The zero crossings in hourly *Dst* index (Figure 2c, data available from http://wdc.kugi.kyoto-u.ac.jp/dstae/index.html) correspond to sudden storm commencements (SSCs). Other

Table 1. Details of the Main Geomagnetic Storm (GS) Periods During 2008 Days 130-220 (9 May to 7 August)

GS	GS Start/End Day Numbers (Dates)	Day Number (Date) of SSC	Day Number (Date) of Minimum Dst Index	Minimum Dst Index (nT)	GS Class
A1	139.5-148.5 (18-27 May)	140.5 (19 May)	142.2 (21 May)	−29	Weak
B1	148.3-157.3 (27 May to 5 June)	149.3 (28 May)	151.1 (30 May)	−20	Weak
C1	157.8-166.8 (5-14 June)	158.8 (6 June)	160.0 (8 June)	−16	Weak
A2	165.9-174.9 (13-22 June)	166.9 (14 June)	167.3 (15 June)	−41	Class 2 moderate
B2	175.8-184.8 (23 June to 2 July)	176.8 (24 June)	177.2 (25 June)	−29	Weak
C2	186.5-195.5 (4-13 July)	187.5 (5 July)	189.3 (7 July)	−10	Weak
A3	193.2-202.2 (11-20 July)	194.2 (12 July)	194.4 (12 July)	−34	Class 2 moderate
B3	203.9-212.9 (21-30 July)	204.9 (22 July)	206.0 (24 July)	−27	Weak

SSCs are not clearly observed as zero crossings in Dst due to overlap between geomagnetic storms or the weakness of the magnetic perturbations. We identify eight geomagnetic storms where zero crossings in Dst coincide with increases in solar wind velocity, 3-hourly Kp index >2 (Figure 2e, data available from http://spidr.ngdc.noaa.gov/spidr/), and increases in 3-hourly Ap index (Figure 2f, data available from http://spidr.ngdc.noaa.gov/spidr/). We define each storm as a 9 day period, starting 24 h before SSC, for the superposed epoch analysis described in section 4.3. The observed storms appear to be in three recurrent sequences (A, B, and C), labeled in Figure 2d according to the first (A1, B1, C1), second (A2, B2, C2), and third (A3, B3) recurrences.

[19] The details of the geomagnetic storms are listed in Table 1, including the storm category based on the minimum Dst index value [*Yokoyama and Kamide*, 1997]. The largest storm disturbance occurred during geomagnetic storm A2 with minimum $Dst = −41$ nT and $Kp >5$ indicating minor (G1) storm conditions. During the rest of the period, Kp is in the range 0-4, below the strict definition of geomagnetic storm levels (G0 on the NOAA Space Weather Scale, http://www.swpc.noaa.gov/NOAAscales/).
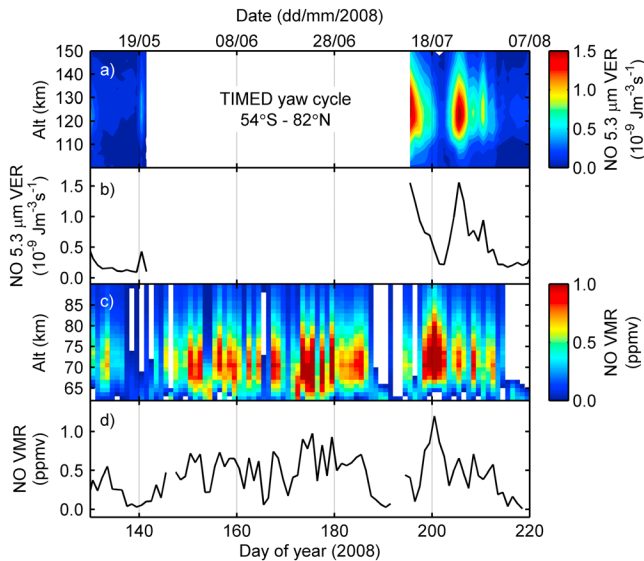
[20] The daily mean GOES >0.6 MeV electron flux (Figure 2g) increases during geomagnetic storm periods A1, B1, C1, A2, B2, A3, and B3. The daily mean GOES >2.0 MeV electron flux (Figure 2h) is much lower than the flux of >0.6 MeV electrons and increases during storm periods A1, A2, A3, and B3. Throughout days 196-202, the flux of >2.0 MeV electrons from the radiation belts observed by GOES was over two orders of magnitude higher than background quiet-time levels. The increases in GOES >0.6 MeV electron flux lag the solar wind velocity by 1-3 days, and the >2.0 MeV electron flux shows a further delay of up to 24 h.

3.2. NO Data

[21] The ground-based microwave observations for 2008 days 130-220 are compared in Figure 3 with NO 5.3 μm volume emission rate (VER) data for the lower thermosphere (100-150 km) from the SABER satellite instrument
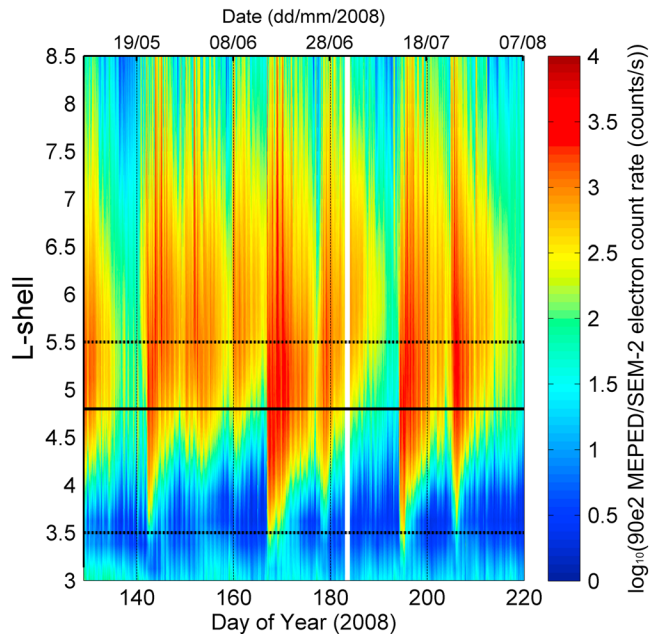

Figure 3. (a) Daily mean SABER NO 5.3 μm VER for 65° S–75°S, (b) daily mean SABER NO 5.3 μm VER for 65° S–75°S averaged over 120–130 km, (c) daily mean NO VMR, and (d) daily mean NO VMR averaged over 65–80 km. VER is given in SI units, where 10^{-9} Jm^{-3} s$^{-1} \equiv 10^{-8}$ erg/(cm^{3}s).

Figure 4. Daily mean MEPED/SEM-2 trapped and quasi-trapped electron count rates for the >100 keV (90e2) channel over $L=3.0$ to $L=8.5$. The horizontal solid black line indicates the L shell ($L=4.8$) corresponding to Troll, Antarctica. The horizontal dashed black lines show the boundaries of the $L=3.5$ to $L=5.5$ range of MEPED/SEM-2 electron data used in this work.
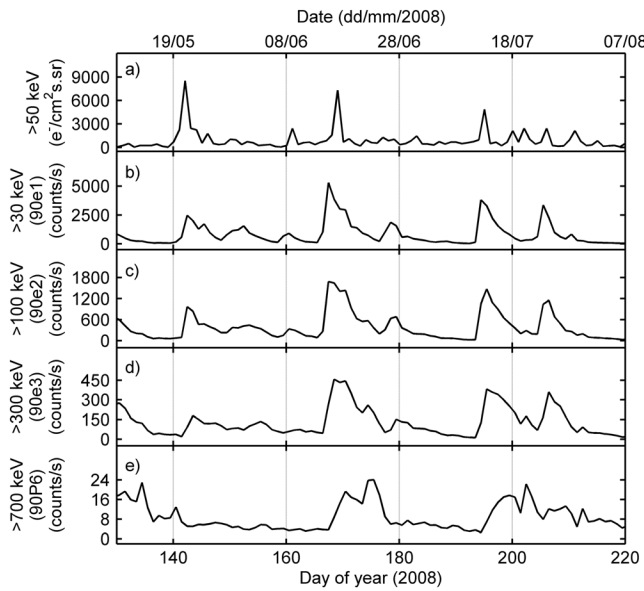
Figure 5. (a) Daily mean AARDDVARK >50 keV electron flux for the $L=3.0$ to $L=7.0$ NAA-SGO conjugate path and daily mean MEPED/SEM-2 trapped and quasi-trapped electron count rates over $L=3.5$ to $L=5.5$ for the (b) >30 keV (90e1), (c) >100 keV (90e2), (d) >300 keV (90e3), and (e) >700 keV (90P6) channels.

[*Mlynczak*, 1997]. The NO VER depends on NO abundance, the kinetic temperature, exothermic production of NO vibrational levels, and the abundance of atomic oxygen. Between days 142 and 194, SABER was viewing 54°S–82°N due to the TIMED yaw cycle and NO VER data over the zonal range 65°S–75°S are unavailable. After this period, enhanced NO VER can be seen (Figure 3a) at altitudes above 110 km where significant nonlocal thermodynamic equilibrium 5.3 μm radiance occurs and can be measured by SABER. This occurs most strongly between days 195–196 and days 204–205, when the daily mean VER averaged over 120-130 km (Figure 3b) exceeds 1.0×10^{-9} Jm^{-3}s^{-1}.

[22] The radiometer observations (Figures 3c and 3d) show periods of enhanced NO at altitudes in the range 65-85 km. Particularly striking features are that the mesospheric NO VMR at 65–80 km is above 0.5 ppmv during much of the 2 month period between days 150 and 212, and the highest value (1.2 ppmv) occurs on day 200 when the thermospheric NO VER observed by SABER is low.

3.3. Electron Data From AARDDVARK and MEPED/POES

[23] A color contour plot of the daily mean MEPED/SEM-2 trapped and quasi-trapped electron count rates for the >100 keV channel during 2008 days 130-220 is shown in Figure 4. The electron count rate exceeds 1000 counts/s
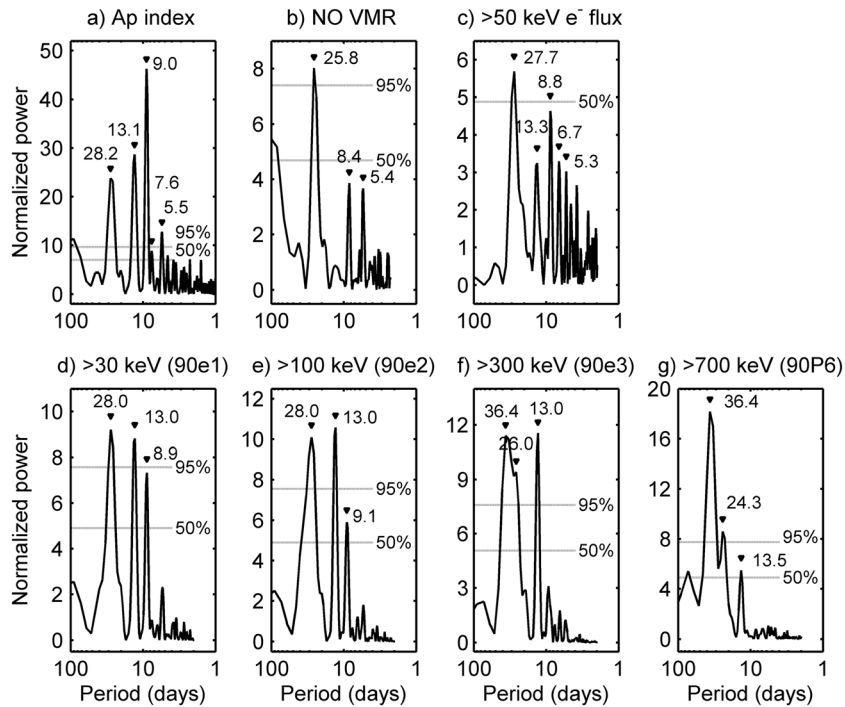

Figure 6. Lomb normalized periodograms for 2008 days 130 to 220 for (a) 3-hourly *Ap* index, (b) daily mean NO VMR averaged over 65–80 km, (c) daily mean AARDDVARK >50 keV electron flux for the $L=3.0$ to $L=7.0$ NAA-SGO conjugate path, and daily mean MEPED/SEM-2 trapped and quasi-trapped electron count rates over $L=3.5$ to $L=5.5$ for the (d) >30 keV (90e1), (e) >100 keV (90e2), (f) >300 keV (90e3), and (g) >700 keV (90P6) channels. The horizontal dotted lines show the 50% and 95% confidence limits.
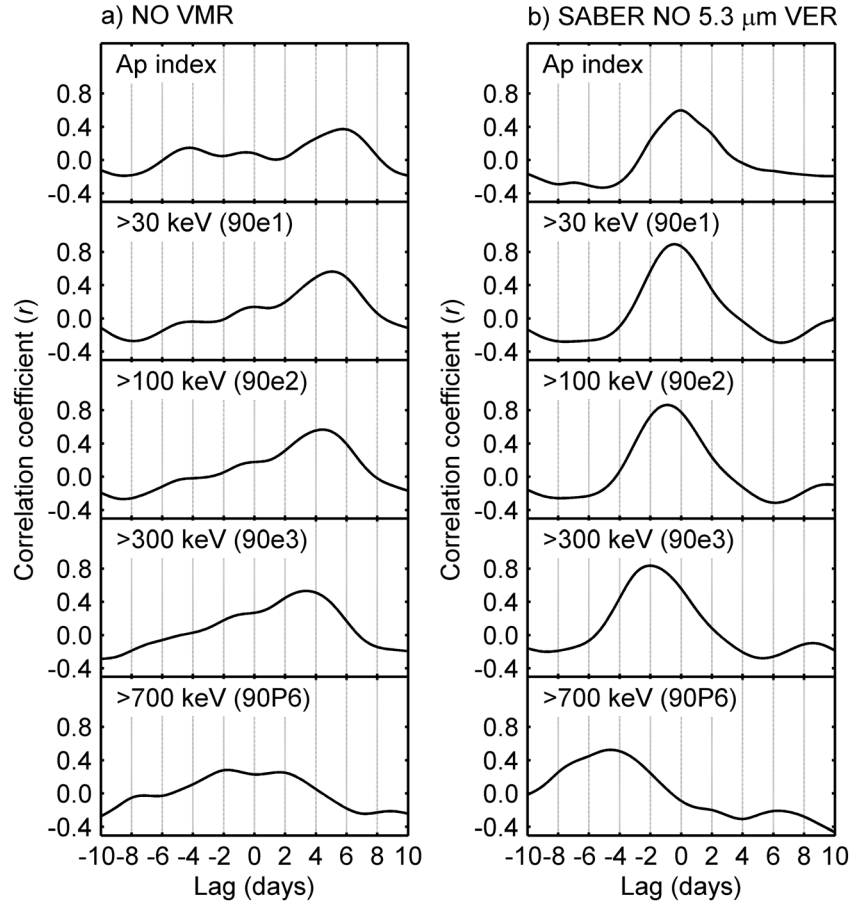
Figure 7. Correlations between (a) daily mean NO VMR averaged over 65-80 km, (b) daily mean SABER NO 5.3 μm VER for 65°S–75°S averaged over 120-130 km, and time-shifted daily mean Ap index and daily mean MEPED/SEM-2 trapped and quasi-trapped electron count rates over $L = 3.5$ to $L = 5.5$ for the >30 keV (90e1), >100 keV (90e2), >300 keV (90e3), and >700 keV (90P6) channels. Positive (negative) lag times occur where NO changes after (before) changes in Ap index or electron count rate.

between $L = 4$ and 6 at the start of the 90 day period, due to an earlier geomagnetic storm. After day 140, the electron count rate increases following each increase in geomagnetic activity. The highest electron count rates for the >100 keV channel exceed >1000 counts/s for $4.0 < L < 8.0$ following each recurrence of the first geomagnetic storm (i.e., A1, A2, and A3). Following each recurrence of the second geomagnetic storm (i.e., B1, B2, and B3), the electron count rate exceeds 1000 counts/s over a narrower range of geomagnetic latitudes, $4.5 < L < 8.0$. For the third recurrent storm (C1 and C2), the maximum electron count rate is lower than for the first two recurrent storms with the largest increase at $L \geq 5.0$. Thus, the third recurrent storm is expected to make only a small contribution to electron ionization at $L = 4.8$, which corresponds to the location of our NO observations. Our analysis uses MEPED/SEM-2 data for the >100 keV and other electron channels over $L = 3.5$-5.5.

[24] A plot of daily mean AARDDVARK >50 keV electron flux for the $L = 3.0$-7.0 NAA-SGO conjugate path is shown in Figure 5a. The main peaks, on days 142, 168, and 194, correspond to the first recurrent storm (i.e., A1, A2, and A3). The electron counts decrease with increasing energy for the four MEPED/SEM-2 channels (Figures 5b-5e), with maximum counts in the >700 keV

channel 200 times smaller than those in the >30 keV channel. The count rates on each channel at the start of the period are elevated due to a geomagnetic storm that started before day 130. The peaks in electron count rate follow increases in geomagnetic activity but are delayed with increasing MEPED/SEM-2 energy channel, as reported previously [*Rodger et al.*, 2010]. Increases in the >700 keV

Table 2. Maximum Correlation Coefficients (r_{max}) and Lag Times Between (a) Time-Shifted Daily Mean NO VMR Averaged Over 65-80 km, (b) Time-Shifted Daily Mean SABER NO 5.3 μm VER for 65°S–75°S Averaged Over 120-130 km, and Daily Mean Ap Index and Daily Mean MEPED/SEM-2 Trapped and Quasi-trapped Electron Count Rates Over $L = 3.5$-5.5

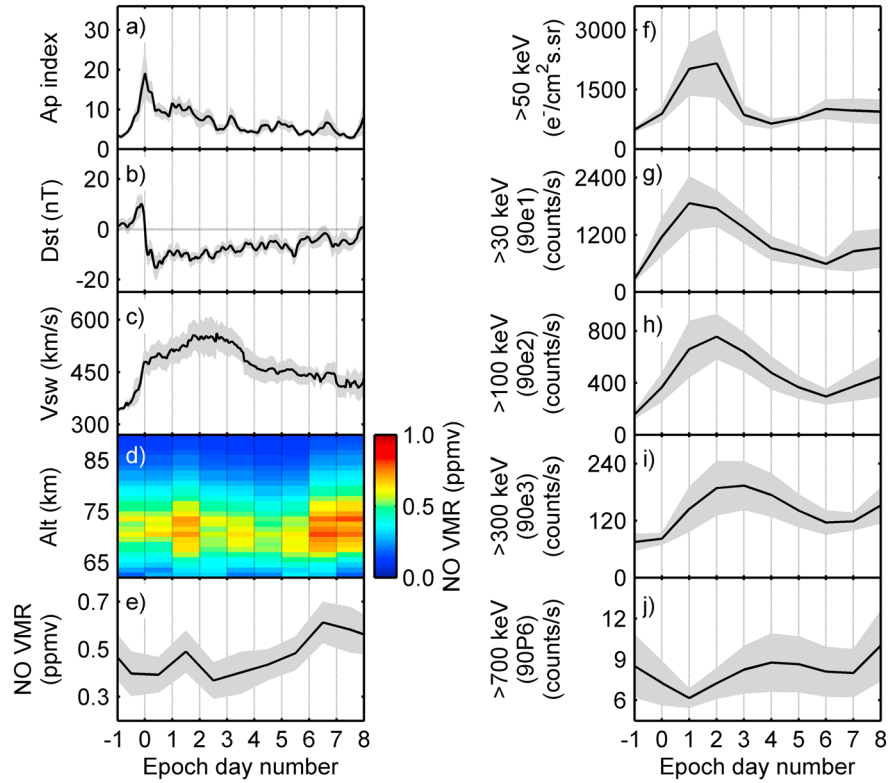|	(a)		(b)	
Parameter	r_{max}	Lag Time (Days)	r_{max}	Lag Time (Days)
Ap index	0.37	5.8	0.60	0.0
>30 keV (90e1)	0.56	5.1	0.89	−0.5
>100 keV (90e2)	0.57	4.4	0.86	−0.9
>300 keV (90e3)	0.53	3.4	0.84	−2.0
>700 keV (90P6)	0.28	−1.8	0.52	−4.6
	0.26	1.6		

Figure 8. Superposed epoch analysis for geomagnetic storm periods (SEA-GS) showing (a) 3-hourly *Ap* index, (b) hourly *Dst* index (c) hourly solar wind velocity (*V*sw), (d) daily mean NO VMR, (e) daily mean NO VMR averaged over 65–80 km, (f) daily mean AARDDVARK >50 keV electron flux for the $L = 3.0$ to $L = 7.0$ NAA-SGO conjugate path, and daily mean MEPED/SEM-2 trapped and quasi-trapped electron count rates over $L = 3.5$ to $L = 5.5$ for the (g) >30 keV (90e1), (h) >100 keV (90e2), (i) >300 keV (90e3), and (j) >700 keV (90P6) channels. Standard errors are shown by the grey shading.

electron channel count rate centered on days 173 and 200 persist for ~9 days each, are associated with geomagnetic storms A2 and A3, and overlap days 173-175 and 198-202 when NO VMR at ~73 km measured by the radiometer was highest.

4. Data Analysis

4.1. Lomb Normalized Periodograms

[25] Following *Mlynczak et al.* [2007], we calculate Lomb normalized periodograms (LNP) for the time series of *Ap* index, NO VMR, AARDDVARK >50 keV electron flux, and MEPED/SEM-2 trapped and quasi-trapped electron count rates. The SABER NO VER data are not included in this analysis due to the large gap in observational data for the SH polar region during this 90 day period. The results of each LNP analysis are shown in Figure 6, with the 50% and 95% significance levels calculated according to the null hypothesis that the data are independent Gaussian random values.

[26] The LNP for *Ap* index (Figure 6a) is similar to that found by *Mlynczak et al.* [2008] for the *Ap* and *Kp* time series covering nearly 5 years from 2002 to 2006. The peaks show periods close to fractions of the typical 27 day solar rotation with a very strong 9.0 day frequency, corresponding to periodicity in the occurrence of high-speed solar wind events [*Verma and Joshi*, 1994] and of coronal hole features on the Sun during 1998–2006 [*Temmer et al.*, 2007].

[27] The LNP for NO VMR averaged over 65–80 km (Figure 6b) shows a 25.8 day periodicity, exceeding the 95% confidence limit, with additional peaks at 8.4 days and 5.4 days. The mesospheric NO periodicity is likely to be dominated by the two periods (days 173–175 and 198–202) of highest NO abundance which are separated by ~26 days. The AARDDVARK >50 keV electron flux (Figure 6c) shows strongest periodicity at 27.7 days, above the 50% confidence limit, and at 8.8 days. The LNP for MEPED/SEM-2 count rates (Figures 6d-6g) show peaks close to the 27 day solar rotation period and at ~13.0 days. The >30 keV and >100 keV channel data also show ~9 day peaks exceeding the 50% confidence limit. For the >300 keV and >700 keV channels, the 9 day peak is less significant but both channels have significant ~13.0-13.5 day recurrence and a peak exceeding the 95% confidence level at 36.4 days that arises from the contribution of electron counts between days 130 and 140.

4.2. Correlation Lag

[28] Correlation coefficient values were calculated by comparing the daily mean NO VMR and SABER NO VER data sets with *Ap* index and the MEPED/SEM-2 electron count rates shifted by a range of lag times. For SABER NO VER, there are 38 days of data available for correlation. The correlation-lag plots are shown in Figure 7, where positive (negative) lag times occur when NO changes after (before)
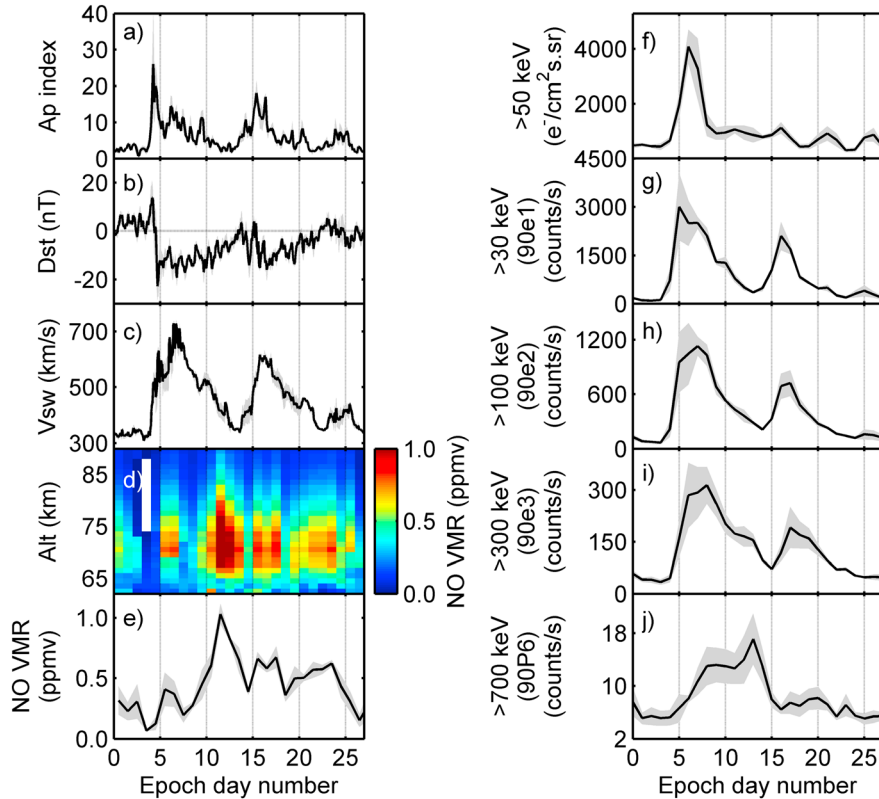
Figure 9. Superposed epoch analysis for Carrington rotation cycles (SEA-CR) showing (a) 3-hourly *Ap* index, (b) hourly *Dst* index (c) hourly solar wind velocity (*V*sw), (d) daily mean NO VMR, (e) daily mean NO VMR averaged over 65–80 km, (f) daily mean AARDDVARK >50 keV electron flux for the $L=3.0$ to $L=7.0$ NAA-SGO conjugate path, and daily mean MEPED/SEM-2 trapped and quasi-trapped electron count rates over $L=3.5$ to $L=5.5$ for the (g) >30 keV (90e1), (h) >100 keV (90e2), (i) >300 keV (90e3), and (j) >700 keV (90P6) channels. Standard errors are shown by the grey shading.

changes in *Ap* index or electron count rate. Details of the maximum correlation coefficients found for each of the lag curves are given in Table 2. A *t* statistic with $n-2$ degrees of freedom, where *n* is the number of samples, was used to test the hypothesis of no correlation. For all correlation coefficient maxima, the statistical significance is >95%. The variability in SABER NO 5.3 μm VER precedes changes in the MEPED/SEM-2 electron channel count rates, leading to negative lag times. The highest correlation ($r_{max}=0.89$) is between SABER NO 5.3 μm VER and the >30 keV electron channel, but the NO VER precedes the >30 keV electrons by 0.5 day. However, the main source of NO at 110-130 km is likely to be low energy (1-10 keV) auroral electrons, for which flux increases typically occur within 0.5 day of increases in *Ap* index, rather than >30 keV EEP which produces maximum ionization at ~95 km [*Turunen et al.*, 2009]. For the radiometer NO VMR data, the highest correlations are with the >30 keV electron channel ($r_{max}=0.56$, lag time of 5.1 days) and >100 keV electron channel ($r_{max}=0.57$, lag time of 4.4 days). This suggests that a significant source of the NO observed by the radiometer could be production in the upper mesosphere by ~30-100 keV electrons followed by downward transport over ~4-5 days to 65-80 km. The small but nonzero correlation (two peaks, one with $r_{max}=0.28$, lag time of -1.8 days and the other with $r_{max}=0.26$, lag time of 1.6 days) between NO VMR and the

>700 keV electron channel data may suggest a contribution to the NO observed by the radiometer from local ionization at 65-80 km.

4.3. Superposed Epoch Analyses

[29] We have carried out two superposed epoch analyses, one (hereafter called "SEA-GS") using the eight identified geomagnetic storm periods and the other (hereafter called "SEA-CR") for the three Carrington rotations 2070-2072. By comparing the results of these two separate analyses, in which the data sampling and superposing differ, we can draw more robust conclusions from a limited data set that contains small numbers of epochs.

[30] The SEA-GS results, where day 0 is determined from the zero crossings in hourly *Dst* index, are shown in Figure 8. The standard errors shown indicate the variability in the superposed data from the eight geomagnetic storms rather than measurement uncertainties. The superposed *Ap* index, *Dst* index, and solar wind velocity data (Figures 8a-8c) show the geomagnetic disturbance lasts for ~8 days following the SSC at epoch day number 0. Two pulses of enhanced NO VMR (Figures 8d and 8e) occur. The first increase at 65-80 km starts 1 day after the geomagnetic storm commences and lasts ~2-3 days. This pulse coincides most closely with increased AARDDVARK >50 keV electron flux and count rates for the >30 keV, >100 keV, and
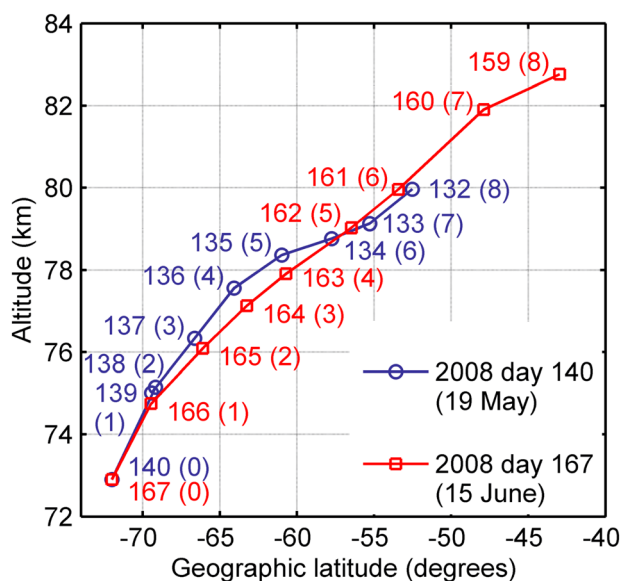
Figure 10. SD-WACCM TEM 8 day backward trajectories from an altitude of 73 km and geographic latitude 72°S for 2008 days 140 (19 May) and 167 (15 June). Each point is labeled with day number (backward trajectory day).

>300 keV electron channels (Figures 8f-8i). The second, stronger NO VMR enhancement starts on epoch day 5 and exceeds 0.5 ppmv over days 6-8. NO VMR reaches a maximum during day 6, between 2 and 5 days after maxima in the observed electron flux and count rates (Figures 8f-8j), and 1-2 days before the highest count rate for the >700 keV electron channel.

[31] The SEA-CR results are shown in Figure 9. The *Ap* index, *Dst* index, and solar wind velocity data (Figures 9a-9c) show peaks corresponding to the three main recurrent geomagnetic storms in each 27 day period, with the first two superposed storms more intense than the third. Four pulses of NO VMR ≥0.3 ppmv occur (Figures 9d and 9e). The first and third NO enhancements at 65-80 km peak on epoch days 5-6 and 15-17, respectively and coincide with increased AARDDVARK >50 keV electron flux and count rates for the >30 keV, >100 keV, and >300 keV electron channels (Figures 9f-9i). The second NO peak exceeds 1 ppmv on epoch days 11 and 12, overlapping increased count rates for the >700 keV electron channel (Figure 9j). The fourth NO maximum, on days 21-24, does not overlap significant increased count rate for any of the MEPED/SEM-2 electron channels. A number of factors may give rise to the delay between increased >700 keV electron counts and increased NO VMR. For example, *Turunen et al*. [2009] showed that when a continuous source of high-energy electron precipitation is applied to the atmosphere it can take 3 days for NO to accumulate to significant levels at altitudes of 70 km, even without transport. It is unlikely that high-energy precipitation >300 keV over Troll is continuous since there are significant magnetic local time variations in the wave-particle interactions responsible for the precipitation. Also, the precipitation will extend over an area in latitude and longitude where the air masses undergo transport, giving rise to NO variations. Thus, the observed delay may be partly due to modulations

in the precipitating electron flux, transport, and the timescale for the atmosphere to respond.

5. Discussion

[32] Both the SEA-GS and SEA-CR analyses show two pulses of increased NO at 65-80 km during each recurrent geomagnetic storm. The first NO pulse occurs 1 day after the geomagnetic storm and follows increases in MEPED/SEM-2 and AARDDVARK electron fluxes in the energy range ~30 keV-300 keV. The 65-80 km altitude corresponds to a peak in ionization by ~200 keV electrons [*Turunen et al*., 2009], suggesting that direct production by electrons with this energy or higher is the source of the first NO pulse. Our analysis provides evidence that the second NO pulse, 5-8 days after the geomagnetic storm, is produced directly by high-energy (>200 keV) electrons. However, our zonal average MEPED/SEM-2 data exclude the region where the 90° electron telescope measurements could be affected by the SAA, including Troll. If the flux of higher-energy (300 keV to several MeV) electrons precipitating into the region poleward of the SAA is higher than outside of this region, as has been shown [*Horne et al*., 2009], then our analysis significantly underestimates the count rate of electrons above Troll that would produce NO directly at 65-80 km. Higher-energy >700 keV electrons would also generate NO_2 and NO_y species below ~65 km, but these species are not currently observed by our radiometer.

[33] Another potential indirect source of the observed mesospheric NO is production above ~82 km by <100 keV electrons followed by transport. We estimate the large-scale meridional and vertical advection of air masses due to the combined effects of zonally averaged winds and wave momentum transport using the National Center for Atmospheric Research Whole Atmosphere Community Climate Model with Specified Dynamics (SD-WACCM) [*Lamarque et al*., 2012; *Straub et al*., 2012]. Transformed Eulerian mean (TEM) backward trajectories (Figure 10) for the zonal mean circulation starting at 72°S and 73 km are calculated using daily TEM velocities determined from daily-averaged WACCM model output as described by *Smith et al*. [2011]. Since the WACCM calculations are the air parcel trajectories, rather than the NO transport trajectories, the amount of NO that the parcel contains will depend upon production within the parcel, advection, and the diffusive entrainment of NO from above and below. Using climatological mixing ratio tendencies for NO due to TEM circulation and the sum of eddy and molecular diffusion contribution in the SH winter [*Smith et al*., 2011], we estimate that at 50°S and an altitude of 82 km the local NO VMR would be increasing by ~70-80% due to transport and ~40% due to diffusion. Further poleward and downward, the contribution from TEM advection is larger. At 73 km over Troll, we estimate the NO VMR changes by ~400% due to TEM advection and ~20% by diffusion. So although the trajectories in Figure 10 are a lower limit to NO transport, TEM advection has at least twice the effect of diffusion at all latitudes and altitudes for air parcels that reach Troll in 5-8 days during SH wintertime. The effect of diffusion would be to upturn the curves to higher altitudes at lower latitudes. Allowing for diffusion, for both of the NO pulse periods considered the majority of the transported NO reaching 73 km above Troll over 5-8 days would originate from a lower

latitude source above 80 km. This matches the lag between increased >100 keV electron count rate and the second NO pulse at 65-80 km. However, it is unclear whether this mechanism could provide a significant contribution to the second NO pulse as it would require substantial production at geographical latitudes equatorward of 60°S. At these lower latitudes, the electron flux is typically much lower than at polar latitudes and the presence of significant sunlight even during the winter months will reduce the lifetime of any NO produced. For example, EEP-related OH enhancements at altitudes of 70–78 km have been found to be largest at geomagnetic latitudes of 55–72° and, in the SH, confined to longitudes between 150°W and 30°E, i.e., poleward of the SAA region [*Andersson et al.*, 2012; *Andersson et al.*, 2013]. Mesospheric NO production would be expected to occur in the same regions as these EEP-driven OH enhancements. The equatorward boundary of the precipitation region, i.e., at longitudes 150°W to 30°E and geomagnetic latitude 55°, corresponds to a geographic latitude of ~65°S. Thus, significant NO generation at geographic latitudes <60°S, followed by transport to Troll station, Antarctica over 5-8 days, appears to be an unlikely source of the observed NO. This supports our analysis indicating that the second NO pulse observed at 65-80 km above Troll station, Antarctica may arise from direct production by >200 keV electrons rather than production by lower energy electrons at higher altitudes and lower latitudes.

6. Conclusions

[34] Pulses of increased mesospheric NO VMR at 65-80 km, reaching ~1.2 ppmv, were observed above Troll station, Antarctica (72°01′S, 02°32′E) ~1-4 days and 5-8 days after small, recurrent geomagnetic storms during the 2008 polar winter. By combining correlation-lag and superposed epoch analyses of the radiometer NO, geomagnetic, and electron data sets, we have identified potential sources of the observed NO. The altitude and time profiles of observed NO and electron data suggest that significant NO may be produced directly in the Antarctic mesosphere at 65-80 km by >200 keV electron precipitation or originate from a source at higher altitudes, e.g., production by >30 keV electrons followed by downward transport. Further work should investigate NO_x production poleward of the SAA region, where the high-energy electron flux can be relatively high, as well as determine transport of this material in the polar middle atmosphere.

References

Andersson, M. E., P. T. Verronen, S. Wang, C. J. Rodger, M. A. Clilverd, and B. R. Carson (2012), Precipitating radiation belt electrons and enhancements of mesospheric hydroxyl during 2004–2009, *J. Geophys. Res.*, 117, D09304, doi:10.1029/2011JD017246.

Andersson, M. E., P. T. Verronen, C. J. Rodger, M. A. Clilverd, and S. Wang (2013), Longitudinal hot-spots in the mesospheric OH variations due to energetic electron precipitation, *Atmos. Chem. Phys. Discuss.*, 13, 19,895–19,919, doi:10.5194/acpd-13-19895-2013.

Barr, R., D. Llanwyn Jones, and C. J. Rodger (2000), ELF and VLF radio waves, *J. Atmos. Sol. Terr. Phys.*, 62, 1689–1718, doi:10.1016/S1364-6826(00)00121-8.

Baumgaertner, A. J. G., A. Seppälä, P. Jöckel, and M. A. Clilverd (2011), Geomagnetic activity related NO_x enhancements and polar surface air temperature variability in a chemistry climate model: Modulation of the NAM index, *Atmos. Chem. Phys.*, 10, 30,171–30,203, doi:10.5194/acpd-10-30171-2010.

Brasseur, G. P., and S. Solomon (2005), *Aeronomy of the Middle Atmosphere*, 3rd ed., Springer, Dordrecht, Netherlands.

Burns, A. G., S. C. Solomon, L. Qian, W. Wang, B. A. Emery, M. Wiltberger, and D. R. Weimer (2012), The effects of corotating interaction region/high speed stream storms on the thermosphere and ionosphere during the last solar minimum, *J. Atmos. Sol. Terr. Phys.*, 83, 79–87, doi:10.1016/j.jastp.2012.02.006.

Clilverd, M. A., A. Seppälä, C. J. Rodger, M. G. Mlynczak, and J. U. Kozyra (2009a), Additional stratospheric NO_x production by relativistic electron precipitation during the 2004 spring NO_x descent event, *J. Geophys. Res.*, 114, A04305, doi:10.1029/2008JA013472.

Clilverd, M. A., et al. (2009b), Remote sensing space weather events: The AARDDVARK network, *Space Weather*, 7, S04001, doi:10.1029/2008SW000412.

Clilverd, M. A., C. J. Rodger, R. J. Gamble, T. Ulich, T. Raita, A. Seppälä, J. C. Green, N. R. Thomson, J.-A. Sauvaud, and M. Parrot (2010), Ground-based estimates of outer radiation belt energetic electron precipitation fluxes into the atmosphere, *J. Geophys. Res.*, 115, A12304, doi:10.1029/2010JA015638.

Daae, M., P. Espy, H. Nesse Tyssøy, D. Newnham, J. Stadsnes, and F. Søraas (2012), The effect of energetic electron precipitation on middle mesospheric night-time ozone during and after a moderate geomagnetic storm, *Geophys. Res. Lett.*, 39, L21811, doi:10.1029/2012GL053787.

Espy, P. J., P. Hartogh, and K. Holmen (2006), A microwave radiometer for the remote sensing of nitric oxide and ozone in the middle atmosphere, *Proc. SPIE*, 6362, 63620P, doi:10.1117/12.688953.

Evans, D. S., and M. S. Greer (2004), *Polar Orbiting Environmental Satellite Space Environment Monitor – 2 Instrument Descriptions and Archive Data Documentation*, NOAA Technical Memorandum version 1.4, Space Environment Laboratory, Boulder, Colo.

Gibson, S. E., J. U. Kozyra, G. de Toma, B. A. Emery, T. Onsager, and B. J. Thompson (2009), If the Sun is so quiet, why is the Earth ringing? A comparison of two solar minimum intervals, *J. Geophys. Res.*, 114, A09105, doi:10.1029/2009JA014342.

Hartogh, P., and G. K. Hartmann (1990), A high-resolution chirp transform spectrometer for microwave measurements, *Meas. Sci. Technol.*, 1(7), 592–595, doi:10.1088/0957-0233/1/7/008.

Harvey, V. L., R. B. Pierce, M. H. Hitchman, C. E. Randall, and T. D. Fairlie (2004), On the distribution of ozone in stratospheric anticyclones, *J. Geophys. Res.*, 109, D24308, doi:10.1029/2004JD004992.

Hibbins, R. E., J. D. Shanklin, P. J. Espy, M. J. Jarvis, D. M. Riggin, D. C. Fritts, and F.-J. Lübken (2005), Seasonal variations in the horizontal wind structure from 0-100 km above Rothera station, Antarctica (67° S, 68° W), *Atmos. Chem. Phys.*, 5, 2973–2980, doi:10.5194/acp-5-2973-2005.

Horne, R. B., et al. (2005), Wave acceleration of electrons in the Van Allen radiation belts, *Nature*, 437, 227–230, doi:10.1038/nature03939.

Horne, R. B., M. M. Lam, and J. C. Green (2009), Energetic electron precipitation from the outer radiation belt during geomagnetic storms, *Geophys. Res. Lett.*, 36, L19104, doi:10.1029/2009GL040236.

Jackman, C. H., D. R. Marsh, F. M. Vitt, R. R. Garcia, C. E. Randall, E. L. Fleming, and S. M. Frith (2009), Long-term middle atmospheric influence of very large solar proton events, *J. Geophys. Res.*, 114, D11304, doi:10.1029/2008JD011415.

Lam, M. M., R. B. Horne, N. P. Meredith, S. A. Glauert, T. Moffat-Griffin, and J. C. Green (2010), Origin of energetic electron precipitation >30 keV into the atmosphere, *J. Geophys. Res.*, 115, A00F08, doi:10.1029/2009JA014619.

Lamarque, J.-F., et al. (2012), CAM-chem: Description and evaluation of interactive atmospheric chemistry in the Community Earth System Model, *Geosci. Model Dev.*, 5, 369–411, doi:10.5194/gmd-5-369-2012.

Lee, J. N., D. L. Wu, G. L. Manney, M. J. Schwartz, A. Lambert, N. J. Livesey, K. R. Minschwaner, H. C. Pumphrey, and W. G. Read (2011), Aura Microwave Limb Sounder observations of the polar middle atmosphere: Dynamics and transport of CO and H_2O, *J. Geophys. Res.*, 116, D05110, doi:10.1029/2010JD014608.

López-Puertas, M., B. Funke, T. Von Clarmann, H. Fischer, and G. P. Stiller (2006), The stratospheric and mesospheric NO_y in the 2002–2004 polar winters as measured by MIPAS/ENVISAT, *Space Sci. Rev.*, 125, 403–416, doi:10.1007/978-0-387-48341-2_32.

Marsh, D. R., S. C. Solomon, and A. E. Reynolds (2004), Empirical model of nitric oxide in the lower thermosphere, *J. Geophys. Res.*, *109*, A07301, doi:10.1029/2003JA010199.

Meredith, N. P., R. B. Horne, M. M. Lam, M. H. Denton, J. E. Borovsky, and J. C. Green (2011), Energetic electron precipitation during high-speed solar wind stream driven storms, *J. Geophys. Res.*, *116*, A05223, doi:10.1029/2010JA016293.

Mlynczak, M., et al. (2003), The natural thermostat of nitric oxide emission at 5.3 μm in the thermosphere observed during the solar storms of April 2002, *Geophys. Res. Lett.*, *30*(21, 2100), doi:10.1029/2003GL017693.

Mlynczak, M. G. (1997), Energetics of the mesosphere and lower thermosphere and the SABER experiment, *Adv. Space Res.*, *20*(6), 1177–1183, doi:10.1016/S0273-1177(97)00769-2.

Mlynczak, M. G., F. J. Martin-Torres, B. T. Marshall, R. E. Thompson, J. Williams, T. Turpin, D. P. Kratz, J. M. Russell III, T. Woods, and L. L. Gordley (2007), Evidence for a solar cycle influence on the infrared energy budget and radiative cooling of the thermosphere, *J. Geophys. Res.*, *112*, A12302, doi:10.1029/2006JA012194.

Mlynczak, M. G., F. J. Martin-Torres, C. J. Mertens, B. T. Marshall, R. E. Thompson, J. U. Kozyra, E. E. Remsberg, L. L. Gordley, J. M. Russell III, and T. Woods (2008), Solar-terrestrial coupling evidenced by periodic behavior in geomagnetic indexes and the infrared energy budget of the thermosphere, *Geophys. Res. Lett.*, *35*, L05808, doi:10.1029/2007GL032620.

Newnham, D. A., P. J. Espy, M. A. Clilverd, C. J. Rodger, A. Seppälä, D. J. Maxfield, P. Hartogh, K. Holmén, and R. B. Horne (2011), Direct observations of nitric oxide produced by energetic electron precipitation into the Antarctic middle atmosphere, *Geophys. Res. Lett.*, *38*, L20104, doi:10.1029/2011GL048666.

Randall, C. E., et al. (2005), Stratospheric effects of energetic particle precipitation in 2003–2004, *Geophys. Res. Lett.*, *32*, L05802, doi:10.1029/2004GL022003.

Randall, C. E., V. L. Harvey, C. S. Singleton, S. M. Bailey, P. F. Bernath, M. Codrescu, H. Nakajima, and J. M. Russell III (2007), Energetic particle precipitation effects on the Southern Hemisphere stratosphere in 1992 – 2005, *J. Geophys. Res.*, *112*, D08308, doi:10.1029/2006JD007696.

Randall, C. E., V. L. Harvey, D. E. Siskind, J. France, P. F. Bernath, C. D. Boone, and K. A. Walker (2009), NO_x descent in the Arctic middle atmosphere in early 2009, *Geophys. Res. Lett.*, *36*, L18811, doi:10.1029/2009GL039706.

Rodger, C. J., M. A. Clilverd, J. C. Green, and M. M. Lam (2010), Use of POES SEM-2 observations to examine radiation belt dynamics and energetic electron precipitation into the atmosphere, *J. Geophys. Res.*, *115*, A04202, doi:10.1029/2008JA014023.

Rothman, L. S., et al. (2009), The HITRAN 2008 molecular spectroscopic database, *J. Quant. Spectrosc. Radiat. Transfer*, *110*, 533–572, doi:10.1016/j.jqsrt.2009.02.013.

Rozanov, E., L. Callis, M. Schlesinger, F. Yang, N. Andronova, and V. Zubov (2005), Atmospheric response to NO_y source due to energetic electron precipitation, *Geophys. Res. Lett.*, *32*, L14811, doi:10.1029/2005GL023041.

Sandford, D. J., C. L. Beldon, R. E. Hibbins, and N. J. Mitchell (2010), Dynamics of the Antarctic and Arctic mesosphere and lower thermosphere—Part 1: Mean winds, *Atmos. Chem. Phys.*, *10*, 10,273–10,289, doi:10.5194/acp-10-10273-2010.

Seppälä, A., C. E. Randall, M. A. Clilverd, E. Rozanov, and C. J. Rodger (2009), Geomagnetic activity and polar surface air temperature variability, *J. Geophys. Res.*, *114*, A10312, doi:10.1029/2008JA014029.

Sheese, P. E., R. L. Gattinger, E. J. Llewellyn, C. D. Boone, and K. Strong (2011), Nighttime nitric oxide densities in the Southern Hemisphere mesosphere–lower thermosphere, *Geophys. Res. Lett.*, *38*, L15812, doi:10.1029/2011GL048054.

Shimazaki, T. (1984), The photochemical time constants of minor constituents and their families in the middle atmosphere, *J. Atmos. Sol. Terr. Phys.*, *46*, 173–191, doi:10.1016/0021-9169(84)90143-0.

Sinnhuber, M., S. Kazeminejad, and J. M. Wissing (2011), Interannual variation of NO_x from the lower thermosphere to the upper stratosphere in the years 1991–2005, *J. Geophys. Res.*, *116*, A02312, doi:10.1029/2010JA015825.

Sinnhuber, M., H. Nieder, and N. Wieters (2012), Energetic particle precipitation and the chemistry of the mesosphere/lower thermosphere, *Surv. Geophys.*, *33*, 1281–1334, doi:10.1007/s10712-012-9201-3.

Siskind, D. E., G. E. Nedoluha, C. E. Randall, M. Fromm, and J. M. Russell III (2000), An assessment of southern hemisphere stratospheric NO_x enhancements due to transport from the upper atmosphere, *Geophys. Res. Lett.*, *27*, 329–332, doi:10.1029/1999GL010940.

Smith, A. K., R. R. Garcia, D. R. Marsh, and J. H. Richter (2011), WACCM simulations of the mean circulation and trace species transport in the winter mesosphere, *J. Geophys. Res.*, *116*, D20115, doi:10.1029/2011JD016083.

Solomon, S. C., C. A. Barth, and S. M. Bailey (1999), Auroral production of nitric oxide measured by the SNOE satellite, *Geophys. Res. Lett.*, *26*, 1259–1262, doi:10.1029/1999GL900235.

Solomon, S., P. J. Crutzen, and R. G. Roble (1982), Photochemical coupling between the thermosphere and the lower atmosphere: 1. Odd nitrogen from 50 to 120 km, *J. Geophys. Res.*, *87*, 7206–7220, doi:10.1029/JC087iC09p07206.

Straub, C., B. Tschanz, K. Hocke, N. Kämpfer, and A. K. Smith (2012), Transport of mesospheric H_2O during and after the stratospheric sudden warming of January 2010: Observation and simulation, *Atmos. Chem. Phys.*, *12*, 5413–5427, doi:10.5194/acp-12-5413-2012.

Straub, C., P. J. Espy, R. E. Hibbins, and D. A. Newnham (2013), Mesospheric CO above Troll station, Antarctica observed by a ground based microwave radiometer, *Earth Syst. Sci. Data Discuss.*, *6*, 1–26, doi:10.5194/essdd-6-1-2013.

Temmer, M., B. Vrsnak, and A. M. Veronig (2007), Periodic appearance of coronal holes and the related variation of solar wind parameters, *Sol. Phys.*, *241*, 371–383, doi:10.1007/s11207-007-0336-1.

Tsurutani, B. T., E. Echer, and W. D. Gonzalez (2011), The solar and interplanetary causes of the recent minimum in geomagnetic activity (MGA23): A combination of midlatitude small coronal holes, low IMF B_z variances, low solar wind speeds and low solar magnetic fields, *Ann. Geophys.*, *29*, 839–849, doi:10.5194/angeo-29-839-2011.

Turunen, E., P. T. Verronen, A. Seppälä, C. J. Rodger, M. A. Clilverd, J. Tamminen, C.-F. Enell, and T. Ulich (2009), Impact of different precipitation energies on NO_x generation during geomagnetic storms, *J. Atmos. Sol. Terr. Phys.*, *71*, 1176–1189, doi:10.1016/j.jastp.2008.07.005.

Urban, J., P. Baron, N. Lautié, N. Schneider, K. Dassas, P. Ricaud, and J. De La Noë (2004), Moliere (v5): A versatile forward- and inversion model for the millimeter and sub-millimeter wavelength range, *J. Quant. Spectrosc. Radiat. Transfer*, *83*(3–4), 529–554, doi:10.1016/S0022-4073(03)00104-3.

Verma, V. K., and G. C. Joshi (1994), On the occurrence rate of high-speed solar wind events, *Sol. Phys.*, *155*, 401–404, doi:10.1007/BF00680603.

Verronen, P. T., A. Seppälä, M. A. Clilverd, C. J. Rodger, E. Kyrölä, C.-F. Enell, T. Ulich, and E. Turunen (2005), Diurnal variation of ozone depletion during the October–November 2003 solar proton events, *J. Geophys. Res.*, *110*, A09S32, doi:10.1029/2004JA010932.

Villanueva, G., and P. Hartogh (2004), The high resolution chirp transform spectrometer for the SOFIA-GREAT instrument, *Exp. Astron.*, *18*(1-3), 77–91, doi:10.1007/s10686-005-9004-3.

Villanueva, G. L., P. Hartogh, and L. Reindl (2006), A digital dispersive matching network for SAW devices in chirp transform spectrometers, *IEEE Trans. Microwave Theory Tech.*, *54*(4), 1415–1424, doi:10.1109/TMTT.2006.871244.

Yando, K., R. M. Millan, J. C. Green, and D. S. Evans (2011), A Monte Carlo simulation of the NOAA POES Medium Energy Proton and Electron Detector instrument, *J. Geophys. Res.*, *116*, A10231, doi:10.1029/2011JA016671.

Yokoyama, N., and Y. Kamide (1997), Statistical nature of geomagnetic storms, *J. Geophys. Res.*, *102*, 14,215–14,222, doi:10.1029/97JA00903.